





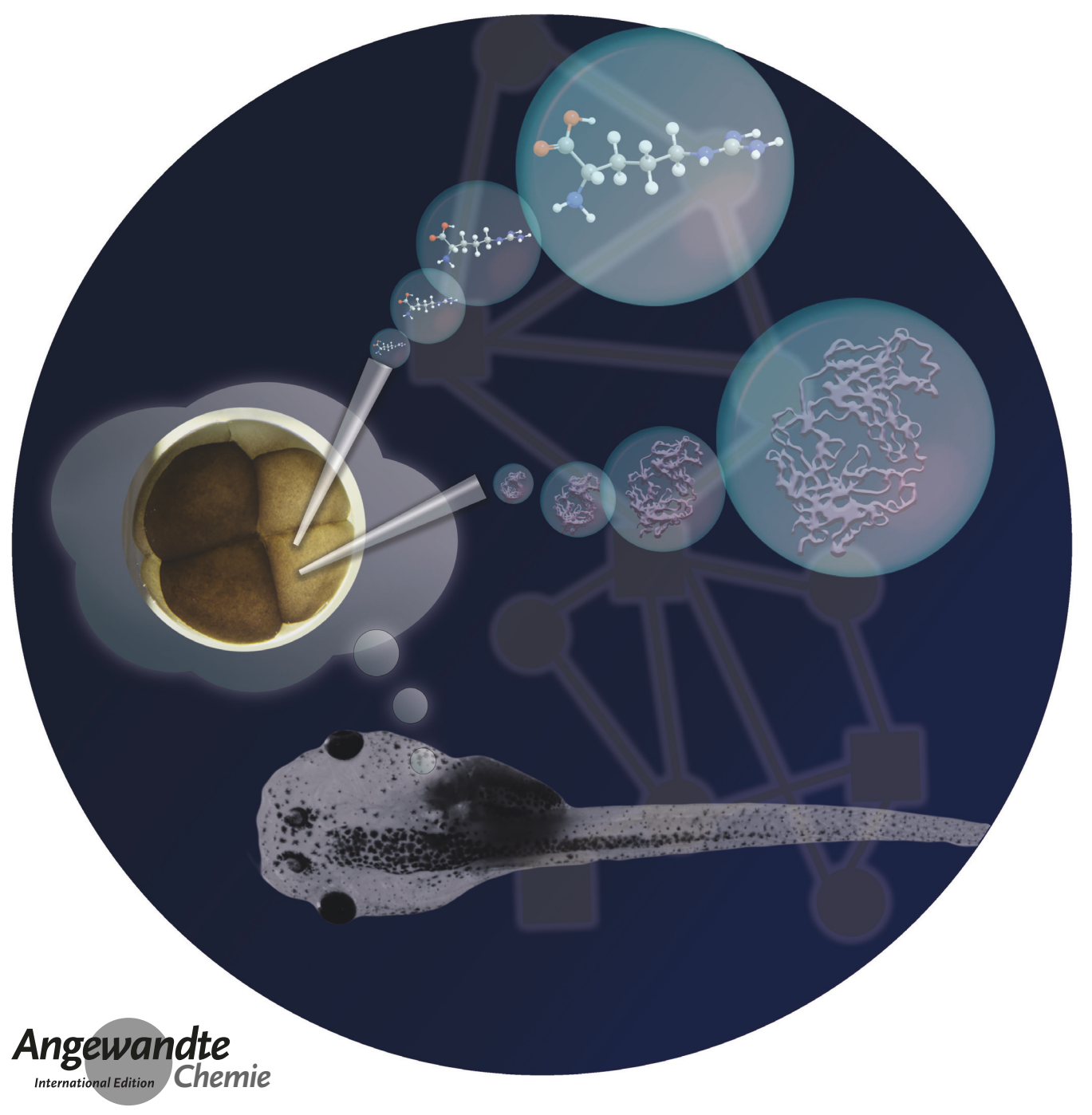


In Vivo Mass Spectrometry Hot Paper

How to cite: Angew. Chem. Int. Ed. 2021, 60, 12852-12858 doi.org/10.1002/anie.202100923 International Edition: German Edition: doi.org/10.1002/ange.202100923

In Vivo Subcellular Mass Spectrometry Enables Proteo-**Metabolomic Single-Cell Systems Biology in a Chordate Embryo Developing to a Normally Behaving Tadpole** (*X. laevis*)**

Camille Lombard-Banek⁺, Jie Li⁺, Erika P. Portero, Rosemary M. Onjiko, Chase D. Singer, David O. Plotnick, Reem Q. Al Shabeeb, and Peter Nemes*





Research Articles



Abstract: We report the development of in vivo subcellular high-resolution mass spectrometry (HRMS) for proteo-metabolomic molecular systems biology in complex tissues. With light microscopy, we identified the left-dorsal and left-ventral animal cells in cleavage-stage non-sentient Xenopus laevis embryos. Using precision-translated fabricated microcapillaries, the subcellular content of each cell was double-probed, each time swiftly (<5 s/event) aspirating <5 % of cell volume $(\approx 10 \text{ nL})$. The proteins and metabolites were analyzed by home-built ultrasensitive capillary electrophoresis electrospray ionization employing orbitrap or time-of-flight HRMS. Labelfree detection of ≈ 150 metabolites (57 identified) and 738 proteins found proteo-metabolomic networks with differential quantitative activities between the cell types. With spatially and temporally scalable sampling, the technology preserved the integrity of the analyzed cells, the neighboring cells, and the embryo. 95 % of the analyzed embryos developed into sentient tadpoles that were indistinguishable from their wild-type siblings based on anatomy and visual function in a background color preference assay.

Introduction

Unbiased measurement of transcripts, proteins, and metabolites in a live cell promises to revolutionize investigations in molecular systems cell biology. Even today, after the invention of single-cell transcriptomics, [11] there exists no single technology capable of the unbiased characterization of both proteins and metabolites in the same single cell in vivo to enable studies at the level of the functioning organisms. While tools of molecular biology and high/super-resolution optical microscopy empowered systems biology for live organisms, they only work for a limited number of gene products at a time that also have to be known ahead of time, thus limiting research scope to targeted studies, typically building on prior knowledge.

Single-cell high-resolution mass spectrometry (HRMS) emerged as a powerful alternative for targeted and untar-

[*] Dr. C. Lombard-Banek, $^{[+]}$ J. Li, $^{[+]}$ Dr. E. P. Portero, C. D. Singer, Prof. Dr. P. Nemes

Department of Chemistry & Biochemistry, University of Maryland 0107 Chemistry Building

8051 Regents Drive, College Park, MD 20742 (USA) E-mail: nemes@umd.edu

Dr. R. M. Onjiko, D. O. Plotnick, R. Q. Al Shabeeb, Prof. Dr. P. Nemes

Department of Chemistry, The George Washington University 800 22nd St NW, Washington, DC 20052 (USA)

Prof. Dr. P. Nemes

Department of Anatomy & Cell Biology, School of Medicine and Health Sciences, The George Washington University 2300 I Street NW, Washington, DC 20037 (USA)

- [+] These authors contributed equally to this work.
- [**] A previous version of this manuscript has been deposited on a preprint server (https://www.biorxiv.org/content/10.1101/2021. 01.19.426900v1).
- Supporting information and the ORCID identification numbers for some of the authors of this article can be found under: https://doi.org/10.1002/anie.202100923.

geted (discovery) studies (reviewed in refs. [1a,b,d,2]). Specialized technologies in cell handling, microscale sample processing, [3] high-efficiency chemical separations, [4] and ion generation extended time-of-flight and orbitrap HRMS instruments to sufficient sensitivity and throughput for single-cell analyses. For example, using nanoHPLC, Nano-POTS enabled the detection of 650 + proteins in single HeLa cells, [3f] which was recently increased to 850+ proteins on a new-generation mass spectrometer. [4c] ScoPE-MS also used nanoHPLC to quantify ≈ 750 proteins from a mammalian cell.[3e] The technology was recently advanced to the quantification of ≈ 1000 proteins/cell. [3e,5] MALDI-TOF followed by nanoLC-HRMS enabled the characterization of lipids, peptides, and proteins in large numbers of single cells dissociated from a rat root ganglion. [6] The data emerging from these and other single-cell studies can be used to derive new hypotheses for biological investigations to establish the functional implications of the observed molecular cell heterogeneity.

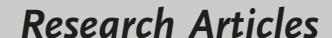
We and others custom-built ultrasensitive capillary electrophoresis (CE) electrospray ionization (ESI) platforms to enable single-cell analyses. These instruments were used to detect transcripts, ≈ 3000 proteins, or ≈ 100 metabolites in single cells/neurons dissected from Aplysia californica, [4a,7] Xenopus laevis embryos, [3a,8] or the rat. [4a] Using capillary microsampling, we extended these measurements to the direct analysis of metabolites^[9] or proteins^[3d] in single cells in early developing X. laevis and zebrafish embryos. Although single-cell HRMS technologies usher an emerging era of multi-omic single-cell 'omics,[10] these tools so far required isolation or sorting of the cells, preventing studies in vivo. We here report the first example of in vivo single-cell HRMS that enables dual proteo-metabolomics of spatiotemporally identified single cells in a live embryo, which freely develops to a visually normally behaving tadpole post analysis.

Results and Discussion

We developed the bioanalytical technology and demonstrated its use in molecular systems cell biology with compatibility for cell, neurodevelopmental, and behavioral biology. Figure 1 presents our analytical and biological tracks, essentially connecting the physical and life sciences. To enable molecular network analyses in live embryos, proteins and metabolites were measured by balancing sensitivity and developmental viability. In the context of developmental neurobiology, the analysis is considered in vivo if the cell is able to heal its membrane, divide, and form progenies for tissue specification and development to give way to a normally behaving organism, viz. a tadpole. The biological trace in the study determined this biological phenotype on the basis of morphological, survival, and behavioral assays. By design, the integration of these tracks generates multi-dimensional metadata to open a window into molecular systems biology and help develop new knowledge and support hypothesisdriven studies.

The vertebrate South African clawed frog (*Xenopus laevis*) was an ideal biological model for technology develop-

12853







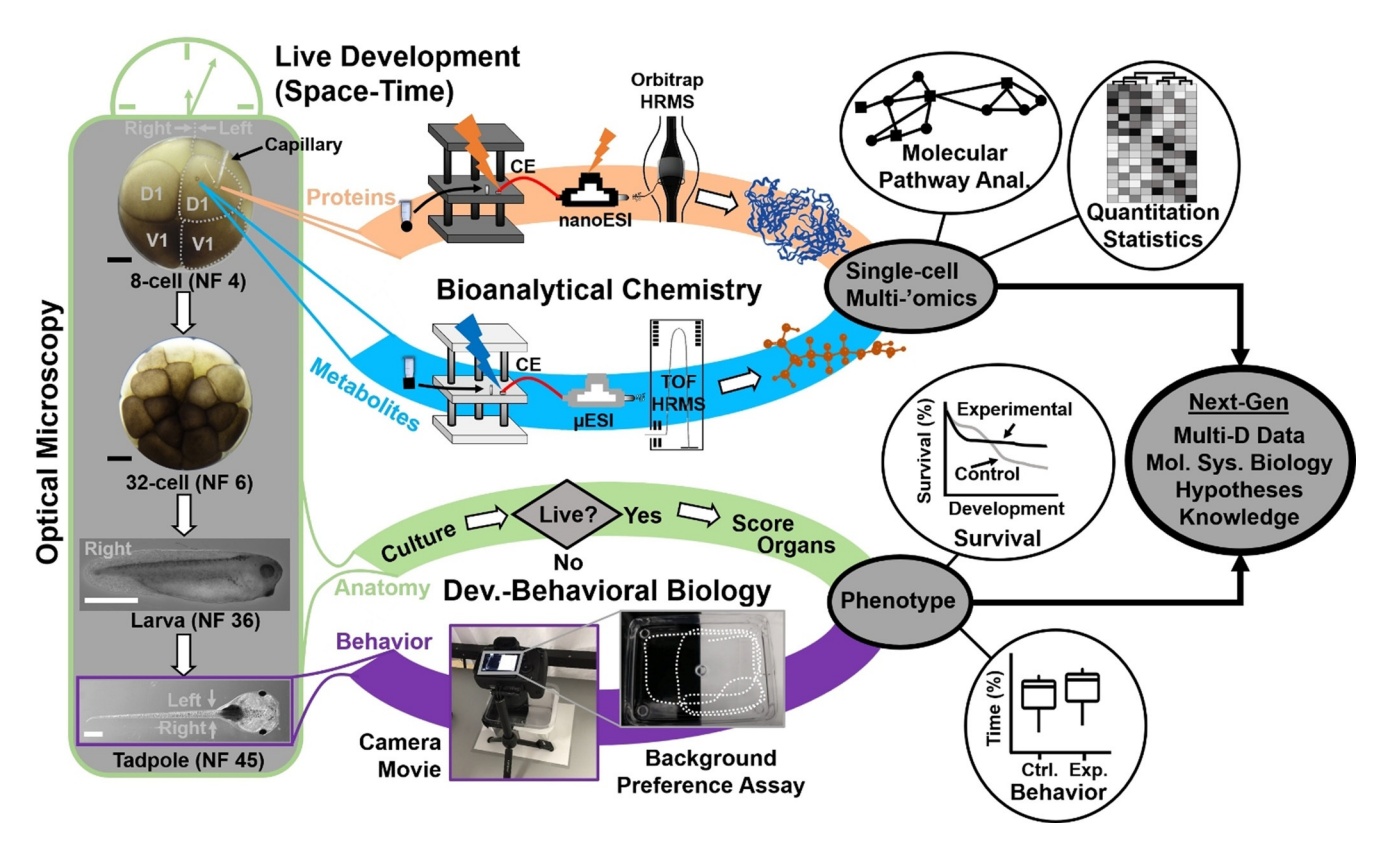


Figure 1. Interdisciplinary strategy enabling in vivo subcellular proteo-metabolomic systems biology with demonstrated compatibility for cell, neurodevelopmental, and behavioral biology using Xenopus laevis as the biological model. As an example, the left dorsal-animal (L-D1) and left ventral-animal (L-V1) cells were identified and the content of each cell rapidly microsampled twice using clean capillaries each time. The collected protein and metabolite samples were analyzed using custom-built ultrasensitive capillary electrophoresis (CE) nano/microflow electrospray ionization (ESI) high-resolution orbitrap and time-of-flight (TOF) mass spectrometry (HRMS). The tadpoles developing from the embryos were characterized for survival, anatomy, and behavior. Scale bars = 250 µm (black), 1 mm (white).

ment, validation, and application in this study. Each cell in the cleavage-stage frog embryo is identifiable based on pigmentation and location and has reproducible tissue fates.[11] Figure 1 exemplifies the identification of the left dorsalanimal (L-D1) and left ventral-animal (L-V1) cells in a live 8cell embryo, which respectively form the neural and epidermal tissues. X. laevis embryos develop externally to the mother and contain considerably large cells (180 nL volume/ cell in the 8-cell embryo), permitting direct inspection and access to the cells. However, the cells populate the embryo in a complex three-dimensional morphology (spherical arrangement) and divide rapidly, in $\approx 15-25$ min per cell cycle between the 2- and 32-cell stages.^[12] These physical characteristics combined with the transient nature of a spatially and temporally developing "embryonic body" fundamentally challenge existing single-cell HRMS technologies in terms of scalability for spatial, temporal, and in vivo operation.

We recognized spatiotemporally scalable sampling as indispensable for this study (Figure 1). While dissociation^[13] and manual dissection^[3a,8a,14] permit cell isolation from the embryo, the former loses spatial information on cell heterogeneity, and the latter requires substantial dexterity and lacks scalability; these features both have important implications in cell and developmental biology. With analyses occurring ex vivo, the current tools exclude the possibility of biological

studies over critical developmental stages, ranging from gastrulation and neurulation to organogenesis and metamorphosis. Likewise, these strategies are incompatible with assessing function and behavior at an organismal level, such as the sentient tadpole. Currently, there exists no single-cell HRMS technology capable of determining the proteo-metabolome of single cells embedded in complex tissues or organisms in vivo with scalability.

We proposed double capillary microsampling as a potential solution for analyzing the cells in vivo. To serve as a micropipette for sample collection, a borosilicate capillary (0.75/1 mm inner/outer diameter) was flame-pulled, then cleaved to a 20-um tip diameter (see SI Methods), and connected to a microinjector delivering negative pressure pulses. The tip of the capillary was inserted into the cell of interest under translation by a precision micromanipulator and guidance by real-time stereomicroscopy. In each of N = 20 stereotypical 8-cell embryos (experimental group), the L-D1 and L-V1 cells were each microsampled twice in a random order with both cells from the same embryo and one sampling for each 'omic analysis. By performing the single-cell analyses exclusively on one side of the embryo (the left, experimental), tissues and organs arising from the nonsampled cells on the other side (right D1, R-D1 and right V1, R-V1) served as the internal control in each embryo to facilitate analysis of



tadpole anatomy (see later). For the control group (Ctrl.), N=20 stereotypical 8-cell embryos were cultured under identical conditions, without microaspiration. This approach was inspired by in situ microprobe sampling that we recently developed for cells in zebrafish and *X. laevis* embryos, albeit functioning only ex vivo and exclusively for metabolomics $^{[3c,9]}$ or proteomics, $^{[3d]}$ but not both 'omes at the same time or on the same cell. The technical details are discussed in the SI document. We experimentally tested that double microsampling using larger capillaries (e.g., $\approx 80~\mu m$ tips) and/or longer aspiration times (scalability) allowed us to aspirate $\approx 100~n L$, viz. 50% of the cell volume. These amounts were sufficient for single-cell HRMS; however, the embryos failed to survive the analysis due to substantial damage by the large capillary (see Figure S1).

To enable cell sampling in vivo in the live embryo, we scaled the approach with assistance from survival assays (Figure 2). Figure S1 presents significant membrane damage on the microsampled cells in a 16-cell embryo before refinement of this approach. In a series of experiments (data not shown), the tip size of the microprobe, the volume collected, and the speed of microsampling were tailored to the cells while monitoring the success of cell divisions after sampling under the stereomicroscope. Each sampling employed a clean and unused capillary to aid cell and embryonic survival by avoiding accidental contamination. Figure 2A tracks the percentage of embryos surviving after ≈ 10 nL, or $\approx 5\%$ of the cell volume, was microaspirated twice from the L-D1 and L-V1 cells (N = 20 embryos). Double microsampling took less than 30 s per cell. By using 20-µm-tip capillaries and conducting two independent sampling events in each cell instead of a single one, we were able to promote cell viability and microhandling of viscous cell contents for downstream sample processing. Embryonic survival was quantified over 7 key stages of vertebrate development: cleavage (Nieuwkoop-Faber, NF 5 and 6), gastrula (NF 10.5, Figure 2B), neurula (NF 13, Figure 2B), early tailbud (NF 22), late tailbud (NF 36 and 41), and tadpole (NF 45, Figure 2B). Compared to 100% of tadpoles successfully developing in the control group (unperturbed wild-type, WT) at all these stages of development, 100% of the embryos developed to the neurula stage and 95% survived to tadpoles in the experimental group. Therefore, capillary microsampling was successfully scaled to preserve viability.

Anatomy was also analyzed for the surviving tadpoles. Figure 2B presents typical examples for tadpoles from the control and experimental groups. Their morphologies were characterized in terms of whole-body length as well as the sizes of the eyes, olfactory organs (Olf.), and total brain, which partially derive from the L-D1 and L-V1 cells (Figure 2B). Body symmetry was also analyzed for the eyes and olfactory tissues along the midline separating the left (experimental) side and the right (control) side (see close-up in Figure 2C). As shown in Figure 2C, the body length (p = 0.315, Mann-Whitney) as well as the center-to-center distances between the eyes (p = 0.411, Mann-Whitney) and the olfactory tissues (p = 0.523, Mann-Whitney) were indistinguishable, as was the total area of the brain (p = 0.121, Mann-Whitney). The size (area) of the eyes (p = 0.142, Wilcoxon signed rank, paired)

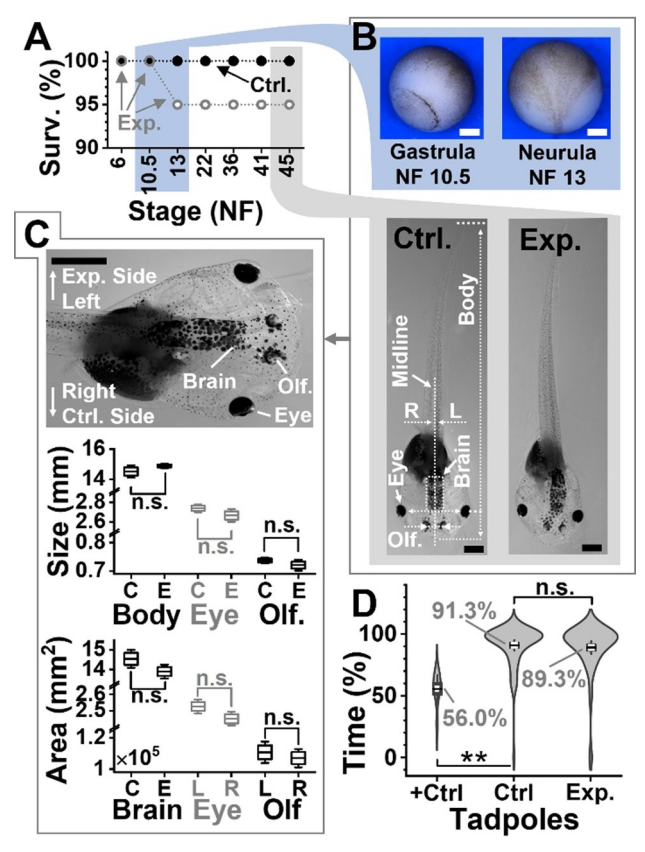
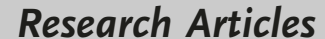


Figure 2. Developmental and behavioral impact of the technology. A) Survival analysis (Surv.) at key developmental stages (NF, Nieuwkoop-Faber) for N = 20 embryos in the control (Ctrl.) group and N = 20embryos in the experimental. B) Representative (top) Ctrl. gastrula and Ctrl. neurula stage embryos and (bottom) Ctrl. and experimental (Exp.) tadpoles. Shown: midline separating left (L)-right (R) axis, body length, brain area, and distance between eyes and olfactory (Olf.) organs. C) Comparison of tadpole anatomy. Top: Close-up image of a tadpole showing the experimental (left) and control (right) side. Right tissues are labeled. Middle: Analysis of organ size on the left (experimental side) between N=5 Ctrl. (C) and N=6 Exp. (E) surviving tadpoles randomly selected. Key: n.s., non-significant, *p < 0.05, Mann-Whitney test. Bottom: Analysis of tissue areas for total brain (Ctrl. vs. Exp. group), the eyes, and the olfactory organs in the 6 Exp. tadpoles. Key: n.s., non-significant, Wilcoxon signed rank, paired). D) Comparison of visual function in a background-color preference assay for $N\!=\!16$ Ctrl. vs. N = 15 Exp. tadpoles. Assay validation via double axotomy of the optic nerves in N = 4 positive Ctrl. tadpoles (+ Ctrl.). Tadpole movies in Videos S1 (Ctrl.) and S2 (+ Ctrl.). Key: n.s., non-significant; *p < 0.05, **p < 0.005 (Mann-Whitney). Scale bars, 250 μ m (white) and 1 mm (black). Box-whisker plots: Box, 1×standard error of the mean (SEM), whiskers: 1.5×SEM.

and olfactory organs (p = 0.142, Wilcoxon signed rank, paired) were also indistinguishable between the experimental and control sides in the tadpoles. Therefore, double subcellular capillary microsampling of the L-D1 and L-V1 in the cleavage-stage embryo led to no detectable impairment on tadpole development, morphologically.

Physical appearance, however, does not equate to performance; therefore, we further evaluated the animals based on behavior. The visual (also including motor, sensory, and neural processing) function was compared at stages 45–50,

12855







when tadpoles display a robust preference for lighter background in a color preference assay^[15] (see setup in Figure 1). The technical details are available in the SI document. Indeed, as shown in Figure 2D, when presented with a dark vs. light background in a tank, the control (WT) tadpoles resided $\approx 91\%$ of the time over the light background (N = 16). These tadpoles recapitulated this robust behavioral phenotype at this stage, [15] thus confirming the robustness of the assay in our hands. We further validated the sensitivity of the assay to detect visual impairment using a positive control (+Ctrl). Tadpoles that underwent double axotomy of their optic nerves (N=4) explored the light background only at \approx 56 % of the time, in a significant difference from the control group $(p = 1.64 \times 10^{-5})$. Indeed, without vision, tadpoles are anticipated to make random explorations, spending $\approx 50\%$ on either side of the tank. These results also agreed with results from an independent investigation, [15] thus confirming that the assay was sufficiently sensitive to detect visual function in our experiments. Swimming $\approx 89\%$ time over the light area, the experimental group (N = 15) presented indistinguishable visual behavior from the control tadpoles (p =0.41, Mann-Whitney). Representative behaviors can be viewed for a Ctrl. and + Ctrl. tadpole in Videos S1 and S2, respectively. Double microsampling of each of the 2 cells in the same embryo preserved embryonic viability and organismal behavior. The approach opened, for the first time in single-cell HRMS, the possibility of dual 'omics of single cells in a live organism, which also undergoes dynamic spatial and temporal reorganization to form a behaving animal, as demonstrated here for the X. laevis embryo and its tadpole in vivo in this work.

Detection of the limited amounts of proteins and metabolites from the cells necessitated ultrasensitive analysis. From each cell type in the same embryo (N=4), the double aspirates were independently processed via a proteomic and metabolomic workflow (recall Figure 1). To eliminate potential systematic biases during sample collection, we randomized the location of subcellular sampling and the order of aspirating the protein and metabolite samples. Each embryo, cell, and processed protein and metabolite sample was assigned a unique identifier in our study, although this information was purposefully not used during data analysis to eliminate potential (conscious or subconscious) biases during sample preparation, processing, or instrumental measurement. This information was only revealed after data collection to aid results interpretation. As detailed in the SI document, each subcellular sample was processed to yield metabolic and proteomic microextracts. For bottom-up proteomics, potential protein losses on vial and pipette tip surfaces were minimized by eliminating the traditional steps of desalting, alkylation, and reduction. The final subcellular samples contained the tryptic digest in $2\,\mu L$ for bottom-up proteomics and 4 µL for metabolomics. To avoid systematic bias during instrumental measurement, the subcellular 'omes were blinded for cell type and analyzed in a randomized order.

With ≈ 100 – $10\,000$ -times smaller amounts of material collected from the cells in this study than those typically processed/measured by standard HPLC-HRMS, we turned to

our ultrasensitive CE-ESI-HRMS instruments for assistance. These platforms provided ≈ 700 zmol sensitivity for peptides on a tribrid quadrupole-orbitrap-ion trap^[3a,d] and ≈ 60 amol sensitivity for metabolites on a quadrupole time-of-flight high-resolution^[8a, 9a] mass spectrometer. The technical details are in the SI document. To facilitate the instrumental measurements, the metabolomic analytical track was limited to cationic electrophoresis in this study. Dual cationic-anionic metabolomics is also possible on these instruments to deepen the detectable portion of the single-cell metabolome. [16] Measurement of $\approx 0.5\%$ (v/v) of the protein extract, thus $\approx 0.03\%$ of the cell's volume, identified 738 proteins (false discovery rate < 1 %), listed in Table S1A. Similarly, analysis of $\approx 0.25\%$ (v/v) of the metabolite sample (volume), viz. \approx 0.01 % of the cell's volume, produced \approx 150 nonredundant metabolic molecular features, 57 of which were identified with a high Level-1^[17] confidence, listed in Table S1B. Notably, detection of these ≈ 800 proteins and metabolites was achieved in an untargeted (discovery) manner, requiring no prior knowledge of cellular composition or the use of functional probes; antibodies or antisense oligos were unnecessary for our technology.

These multi-omics data also opened a window into (sub)cellular biochemistry, directly in the live embryo. Statistical enrichment analysis using the Kyoto Encyclopedia of Genes and Genomes^[18] revealed significant coverage of several known pathways (Figure 3A). The pathway data are listed in Table S2. For example, the arginine-proline pathway, TCA cycle, glycolysis, and pyruvate metabolism were represented with statistical significance, whereas several other amino acid pathways had high pathway impact. Notably, these proteins and metabolites assessed cellular biochemistry in complementary performance. For example, the biosynthesis of aminoacyl-tRNA and valine-leucine-isoleucine was only represented by metabolites, whereas glycolysis/gluconeogenesis was solely enriched for by proteins (see statistics and fold changes in Table S2). Further, other pathways, such as arginine biosynthesis and arginine-proline metabolism, were represented by both 'omes (Table S2). Figure 3B annotates arginine-proline metabolism based on the complementary detection of proteins and metabolites in the cells. The observed coverage of the network raises a potential for studies targeting particular 'omic processes. By also including anionic metabolites during CE-ESI-HRMS in future experiments, we anticipate many other cellular pathways to be detectable by this approach, such as the TCA cycle and energy production as well as drug metabolism. These results illustrate the benefit of measuring more than one 'ome in single cells toward a holistic understanding of cellular systems biology at the molecular level.

Finally, we applied the technology to ask whether the pluripotent cells harbored detectable differences in proteometabolomic activity at such an early stage of development. Although embryonic cells have reproducible tissue fates in the cleavage-stage embryo of Xenopus, unbiased and parallel characterization of their proteome and metabolome has not been possible due to a lack of sufficiently sensitive and specific molecular tools. We relatively quantified ≈ 450 proteins and ≈ 80 metabolites between the L-D1 and L-V1





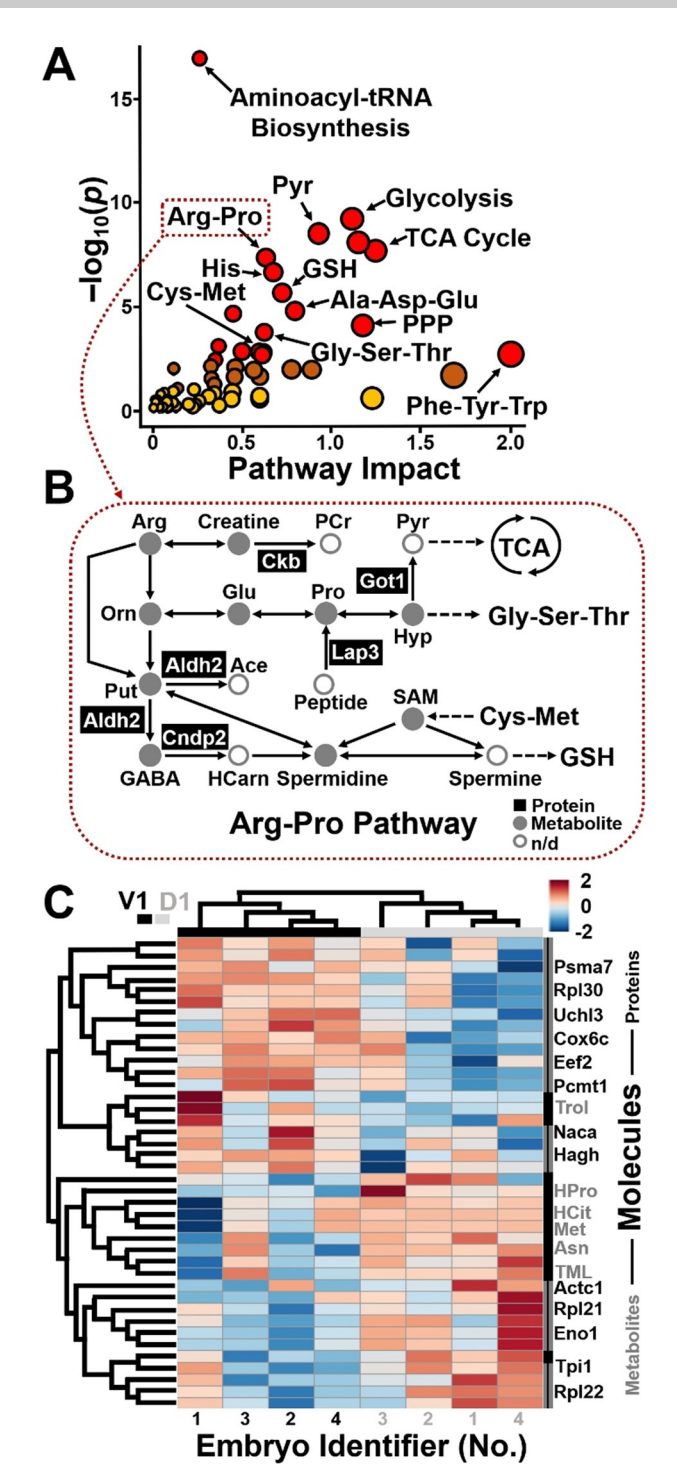


Figure 3. Qualitative and quantitative proteo-metabolomic systems biology on the L-D1 and L-V1 cells in the live embryo. A) KEGG pathway analysis of the identified proteins (Table S1) and metabolites (Table S2). Pathway data are in Table S3. B) Example showing proteins and metabolites with complementary enrichment in the arginine-proline pathway. C) Unsupervised (blinded) hierarchical cluster-heat map analysis of the detected protein and metabolite quantities revealing reproducible, systematic, and significant differences between the cell types. Top 40 most significantly dysregulated molecules shown (p < 0.05, see quantitative statistics in Table S3).

cells in each embryo (N = 4) based on the subcellular HRMS data obtained in this study. Quantification was based on signal abundances in the HRMS datasets (see Methods, SI), which offer an effective and robust proxy for concentration in CE-ESI-HRMS. [3a,4a] Quantified protein and metabolite signals are presented in Table S3.

These quantitative proteo-metabolomic data were evaluated using multivariate data analysis. As highlighted earlier, the phenotypes of the cells or the identifier of each embryo were hidden to ensure bias-free data analysis. Figure 3C presents the unsupervised hierarchical cluster analysis (HCA) and intensity heat map of the data based on the top 40 statistically most significantly dysregulated molecules, including 13 metabolites and 27 proteins. The top dendrogram clusters the samples into two groups in the HCA plot. Upon revealing the identity of the samples, we learned that the groups corresponded to the D1 and V1 cell types. Further, the heatmap revealed notable quantitative molecular differences between the cell types. The left dendrogram organized the proteins and metabolites into two groups in the HCA plot. The HCA heatmap readily captures reproducible abundance differences between the cell types. Specifically, in this map, 20 molecules, containing 10 metabolites and 10 proteins, were more abundant in the L-D1, whereas 20 molecules, encompassing 3 metabolites and 17 proteins were enriched in the L-V1. Table S3 tabulates the proteins and metabolites with statistically ($p \le 0.05$) and biologically significant dysregulation (|fold change| ≥ 1.5). In classical HRMS approaches requiring cell pooling, these intriguing molecular differences between the cell types would have been lost due to averaging across large numbers of cells or known molecular differences between embryos.

Conclusion

We enabled in vivo single-cell proteomics and metabolomics in the same single cell in live chordate embryos using X. laevis as the biological model. The technology revealed quantitative proteo-metabolomic differences between cells at the cleavage stage. These results afford previously unavailable insights into the establishment of cell heterogeneity during embryogenesis; they also challenge our current understanding of the underlying molecular processes. Differential production of these molecules reveals that asymmetry along the dorsal-ventral, one of the three primary axes of the vertebrate body plan, is set up rather early during embryonic development, when transcriptional heterogeneity is not detectable along this axis based on sequencing of the respective single-cell transcriptomes^[19] in *Xenopus*. These findings support our earlier discovery of molecules, such as metabolites, [8a] affecting tissue fates via noncanonical mechanisms of action. Although determining the exact biological significance of these findings goes beyond the scope of this study, the data generated in this work may be used to develop hypotheses for experiments targeting specific proteins and metabolites and their functions.

Supporting future investigations, our technology is scalable in space and time to other types of cells and different biological models. Subcellular HRMS is compatible with complex tissues and live development, as demonstrated for

Research Articles





the live embryo here. It does not escape our attention that our technology can be used to perform multi-'omics on subcellular organelles. Further, the approach is also adaptable to classical and modern tools of biology and health studies, such as optical microscopy and behavioral assays (as demonstrated in this study) to characterize phenotypes as well as established or contemporary tools of molecular biology, including expression/translation-blocking morpholinos or gene editing by CRISPR-Cas9, to probe function. We anticipate in vivo proteo-metabolomic subcellular CE-ESI-HRMS to expand the modern toolbox of cell and developmental biology, neuroscience, and health research. This technology realizes new strengths in the molecular study of the building block of life, the cell, and processes governing the formation of tissues, organs, and entire organisms with complex behavior.

Acknowledgements

This research was partially supported by an Arnold and Mabel Beckman Foundation Beckman Young Investigator award (to P.N.), the National Science Foundation under awards DBI-1826932 (to P.N.) and IOS-1832968 CAREER (to P.N.), and the National Institutes of Health under award 1R35GM124755 (to P.N.). The content presented in this work and the conclusions drawn are solely the responsibility of the authors and do not necessarily represent the official views of the sponsors. We are grateful to Dr. Sally Moody (The George Washington University, Washington, DC) for supplying *X. laevis* embryos for a pilot experiment.

Conflict of interest

The authors declare no conflict of interest.

Keywords: embryos \cdot mass spectrometry \cdot metabolites \cdot proteins \cdot single cells

- a) T. J. Comi, T. D. Do, S. S. Rubakhin, J. V. Sweedler, J. Am. Chem. Soc. 2017, 139, 3920-3929; b) L. Zhang, A. Vertes, Angew. Chem. Int. Ed. 2018, 57, 4466-4477; Angew. Chem. 2018, 130, 4554-4566; c) S. P. Couvillion, Y. Zhu, G. Nagy, J. N. Adkins, C. Ansong, R. S. Renslow, P. D. Piehowski, Y. M. Ibrahim, R. T. Kelly, T. O. Metz, Analyst 2019, 144, 794-807; d) R. T. Kelly, Mol. Cell. Proteomics 2020, 19, 1739-1748.
- [2] a) R. Zenobi, Science 2013, 342, 1243259; b) E. Levy, N. Slavov in Systems Biology, Vol. 62 (Eds.: W. Kolch, D. Fey, C. J. Ryan), Portland Press, London, 2018, pp. 595-605; c) H. Specht, N. Slavov, J. Proteome Res. 2018, 17, 2565-2571.
- [3] a) C. Lombard-Banek, S. A. Moody, P. Nemes, Angew. Chem. Int. Ed. 2016, 55, 2454–2458; Angew. Chem. 2016, 128, 2500–2504; b) I. Virant-Klun, S. Leicht, C. Hughes, J. Krijgsveld, Mol.

- Cell. Proteomics 2016, 15, 2616–2627; c) R. M. Onjiko, E. P. Portero, S. A. Moody, P. Nemes, J. Visualized Exp. 2017, 130, e56956; d) C. Lombard-Banek, S. A. Moody, M. C. Manzini, P. Nemes, Anal. Chem. 2019, 91, 4797–4805; e) B. Budnik, E. Levy, G. Harmange, N. Slavov, Genome Biol. 2018, 19, 161; f) Y. Zhu, G. Clair, W. B. Chrisler, Y. Shen, R. Zhao, A. K. Shukla, R. J. Moore, R. S. Misra, G. S. Pryhuber, R. D. Smith, C. Ansong, R. T. Kelly, Angew. Chem. Int. Ed. 2018, 57, 12370–12374; Angew. Chem. 2018, 130, 12550–12554.
- [4] a) P. Nemes, S. S. Rubakhin, J. T. Aerts, J. V. Sweedler, Nat. Protoc. 2013, 8, 783-799; b) S. Li, B. D. Plouffe, A. M. Belov, S. Ray, X. Wang, S. K. Murthy, B. L. Karger, A. R. Ivanov, Mol. Cell. Proteomics 2015, 14, 1672-1683; c) Y. Z. Cong, Y. R. Liang, K. Motamedchaboki, R. Huguet, T. Truong, R. Zhao, Y. F. Shen, D. Lopez-Ferrer, Y. Zhu, R. T. Kelly, Anal. Chem. 2020, 92, 2665-2671.
- [5] H. Specht, E. Emmott, A. A. Petelski, R. G. Huffman, D. H. Perlman, M. Serra, P. Kharchenko, A. Koller, N. Slavov, *Genome Biology* 2021, 22, 50.
- [6] T. D. Do, J. F. Ellis, E. K. Neumann, T. J. Comi, E. G. Tillmaand, A. E. Lenhart, S. S. Rubakhin, J. V. Sweedler, *ChemPhysChem* 2018, 19, 1180-1191.
- [7] a) T. Lapainis, S. S. Rubakhin, J. V. Sweedler, *Anal. Chem.* 2009, 81, 5858-5864; b) P. Nemes, A. M. Knolhoff, S. S. Rubakhin, J. V. Sweedler, *Anal. Chem.* 2011, 83, 6810-6817; c) J. X. Liu, J. T. Aerts, S. S. Rubakhin, X. X. Zhang, J. V. Sweedler, *Analyst* 2014, 139, 5835-5842.
- [8] a) R. M. Onjiko, S. A. Moody, P. Nemes, *Proc. Natl. Acad. Sci. USA* 2015, 112, 6545-6550; b) C. Lombard-Banek, S. Reddy, S. A. Moody, P. Nemes, *Mol. Cell. Proteomics* 2016, 15, 2756-2768.
- [9] a) R. M. Onjiko, E. P. Portero, S. A. Moody, P. Nemes, *Anal. Chem.* 2017, 89, 7069-7076; b) R. M. Onjiko, D. O. Plotnick, S. A. Moody, P. Nemes, *Anal. Methods* 2017, 9, 4964-4970.
- [10] a) I. C. Macaulay, C. P. Ponting, T. Voet, Trends Genet. 2017, 33, 155–168; b) A. J. Ma, A. McDermaid, J. Xu, Y. Z. Chang, Q. Ma, Trends Biotechnol. 2020, 38, 1007–1022.
- [11] G. Hirose, M. Jacobson, Dev. Biol. 1979, 71, 191-202.
- [12] K. Karimi, J. D. Fortriede, V. S. Lotay, K. A. Burns, D. Z. Wang, M. E. Fisher, T. J. Pells, C. James-Zorn, Y. Wang, V. G. Ponferrada, S. Chu, P. Chaturvedi, A. M. Zorn, P. D. Vize, *Nucleic Acids Res.* 2018, 46, D861 D868.
- [13] J. A. Briggs, C. Weinreb, D. E. Wagner, S. Megason, L. Peshkin, M. W. Kirschner, A. M. Klein, *Science* 2018, 360, 980.
- [14] L. Sun, K. M. Dubiak, E. H. Peuchen, Z. Zhang, G. Zhu, P. W. Huber, N. J. Dovichi, *Anal. Chem.* 2016, 88, 6653–6657.
- [15] A. S. Viczian, M. E. Zuber, J. Visualized Exp. 2014, 88, e51726.
- [16] E. P. Portero, P. Nemes, *Analyst* **2019**, *144*, 892–900.
- [17] A. C. Schrimpe-Rutledge, S. G. Codreanu, S. D. Sherrod, J. A. McLean, J. Am. Soc. Mass Spectrom. 2016, 27, 1897 1905.
- [18] M. Kanehisa, M. Furumichi, M. Tanabe, Y. Sato, K. Morishima, Nucleic Acids Res. 2017, 45, D353 – D361.
- [19] a) M. Flachsova, R. Sindelka, M. Kubista, *Sci. Rep.* 2013, *3*, 2278;
 b) E. De Domenico, N. D. L. Owens, I. M. Grant, R. Gomes-Faria, M. J. Gilchrist, *Dev. Biol.* 2015, *408*, 252–268.

Manuscript received: January 20, 2021 Accepted manuscript online: March 7, 2021 Version of record online: April 8, 2021



Supporting Information

In Vivo Subcellular Mass Spectrometry Enables Proteo-Metabolomic Single-Cell Systems Biology in a Chordate Embryo Developing to a Normally Behaving Tadpole (*X. laevis*)**

Camille Lombard-Banek⁺, Jie Li⁺, Erika P. Portero, Rosemary M. Onjiko, Chase D. Singer, David O. Plotnick, Reem Q. Al Shabeeb, and Peter Nemes^{*}

anie_202100923_sm_miscellaneous_information.pdf anie_202100923_sm_Video_S1.mp4 anie_202100923_sm_Video_S2.mp4

Author Contributions

P.N., C.L.-B., J.L., and E.P.P. designed the research. C.L.-B. and R.Q.A. prepared and C.L.-B. measured the proteomic samples. J.L., E.P.P., R.M.O., and D.P. prepared and J.L. measured the metabolic samples. J.L., E.P.P., C.D.S., and P.N. designed and conducted the survival, anatomical, and behavioral assays. P.N., C.L.-B., and J.L. analyzed the data, interpreted the results, and wrote the manuscript. All the authors commented on the manuscript.

MATERIALS AND METHODS

Materials and Reagents. All reagents and solvents were obtained at reagent grade or higher purity from Fisher Scientific (Pittsburg, PA) unless otherwise noted. Solutions for HRMS were prepared using LC-MS grade solvents and reagents (methanol, acetonitrile, water, formic acid, and acetic acid). For CE, bare fused silica capillaries (40/105 μm inner/outer diameter) were purchased from Polymicro Technologies (Phoenix, AZ) and used after initial conditioning (100 mM sodium hydroxide for 5 min, then rinsed with water). CE micro-flow ESI (CE-μESI) for metabolomics employed a laser-cleaved stainless-steel blunt needle as the spray emitter (130/260 μm inner/outer diameter) from Hamilton Company (Reno, NV). The CE-nanoESI setup for proteomics used a borosilicate capillary (0.75/1 mm inner/outer diameter) tapered on a Flaming/Brown-style capillary puller (P-1000, Sutter Instruments, Novato, CA) and cleaved to a 20-μm tip diameter under a stereomicroscope (model SMZ18, Nikon, Melville, NY).

Solutions. The "metabolite extraction solvent" was an aqueous mixture of 40% (v/v) acetonitrile (ACN) and 40% (v/v) methanol (MeOH) solution, chilled to 4 °C. The "protein extraction—digestion buffer" was 50 mM ammonium bicarbonate in water. For CE, the "background electrolyte (BGE)" was 1% (v/v) formic acid (yields pH 2.8^[1]) for metabolomics and 25% (v/v) MeOH with 1 M formic acid for proteomics (yields pH 1.8). The "CE-µESI sheath solution" was aqueous 50% (v/v) methanol containing 0.1% (v/v) formic acid. The "nanoESI sheath solution" was 10% (v/v) MeOH with 0.05% (v/v) acetic acid.

Animal Care and Embryology. All protocols concerning the humane care and handling of vertebrate *X. laevis* animals were approved by the University of Maryland Institutional Animal Care and Use Committee (IACUC No. R-DEC-17-57). Adult male and female frogs were received from Nasco (Fort Atkinson, WI) and maintained in a breeding colony. Embryos were obtained by gonadotropin-induced natural mating of two sets of parents at ~21 °C, dejellied in 2% cysteine solution, and cultured in 100 % Steinberg's solution (14 °C) following standard protocols. [2] Two-cell embryos displaying stereotypical pigmentation, size, and location [2] were transferred into a Petri dish containing 100% Steinberg's solution. The embryos were monitored under a

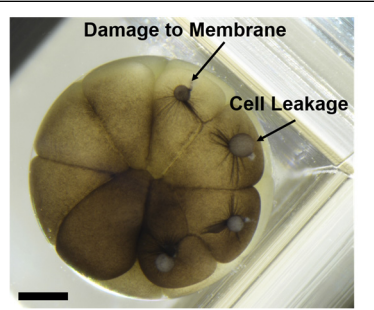


Figure S1. Microsampling was scaled to minimize cell damage. A 16-cell embryo with substantial damage after microsampling before technology refinement. Scale = 250 μm.

stereomicroscope until they reached the 8-cell stage, then the left dorsal-animal (L-D1) and left ventral-animal (L-V1) cells were identified based on reproducible cell-fate maps^[3].

Microprobe Sampling and Sample Processing.

Contents of the L-D1 and L-V1 cells were collected via capillary microsampling^[4] in a randomized order. Microsampling using capillaries with too large tips or delaying aspiration may significantly damage the cell and the developing embryo. For example, in the 16-cell embryo shown in **Figure S1**, the cytoplasm of each cell partially leaked through the hole that was left on the cell membrane as the capillary with too large tip diameter was withdrawn. To promote cell and embryonic

viability post microsampling, the diameter of the capillary tip and duration of sampling were scaled. In this study, the tip of a borosilicate capillary (0.75/1 mm inner/outer diameter) with ~20 μm diameter was fine positioned into the identified cells under control by a three-axis manual micromanipulator (Warner Instruments, Hamden, CT) and guidance by a high-resolution stereomicroscope (SMZ18, Nikon). An ~10 nL portion of the cell was aspirated each time by delivering calibrated pressure pulses (-40 psi) to the microcapillary using a connected microinjector (model PLI-100A, Warner Instruments, Hamden, CT). The total duration of each microsampling was less than ~3 s, separated by an ~ 30 s gap required to install the replacement capillary (for the second sampling). The subcellular aspirates were expelled into individual microvials and processed differently for metabolomic^[4c, 5] and proteomic^[4d] analyses following our established protocols. Metabolites were extracted into 4 μL of metabolite extraction solvent (chilled to 4 °C), facilitated by vortex-mixing for 1 min, and the resulting extract was centrifuged to pellet cell debris (8,000 \times g, 5 min, 4 °C). Proteins were extracted into 5 μ L of protein extraction—digestion buffer, denatured at 60 °C, and digested to peptides with 0.5 μL of 0.5 µg/µL trypsin (37 °C, 5 h). The resulting digests were dried in vacuum at 60 °C. The resulting metabolite and protein samples were stored at -80 °C until analysis.

Behavioral Assays. A portion of the microsampled (wild-type) 8-cell embryos was cultured to the tadpole stage (~21 °C) to study their visual behavior using a background color preference assay. This assay reproducibly and robustly measures the differential preference of tadpoles to spend time over light and dark backgrounds between Nieuwkoop-Faber Stages 45 and 50.^[6] The tadpoles were humanely raised, maintained, and treated following protocols approved by the University of Maryland IACUC (protocol no. R-JUN-20-31). The residence times of each tadpole over the light (white) and dark (black) backgrounds were quantified in a double-tank behavioral system that we built and operated following an established protocol^[6]. The movement of each tadpole was recorded on a digital camera (model EOS 70D, Canon USA Inc.) for 2 min on two occasions per day over 2 days. The videos were recorded at 30 frames per second with Full HD resolution (1920 × 1080 pixel²) and using ALL-I compression. The percentage of time that each tadpole spent in total over the light and dark areas was calculated based on the location of the tadpoles' eyes by manually reviewing the recording, frame by frame, in Windows Media Player version 12 (Microsoft, Redmond, WA). A tadpole was considered to cross the white-black boundary only if both its eyes delineated the boundary.

Validation. The background color preference assay was validated using a positive control (+Ctrl.) group and by comparing results from our study to those independently established by others. [6] The control group (Ctr.) consisted of wildtype (WT) tadpoles (N = 16). The +Ctr group consisted of WT tadpoles (N = 4) one day after double axotomy of the left and right optic nerves following the protocol established in Ref. [6]. The movement of each tadpole was tracked during the background preference assay, as described earlier. Without visual perception, tadpoles were anticipated to randomly explore the white and black areas, viz. spending ~50% of time over either background color. Indeed, in an independent study, tadpoles post double axotomy spent 49–51% of time over the white background (Days 1 to 2), whereas the control explored this area in 99%–79% of time with this difference being statistically significant. [6] In our

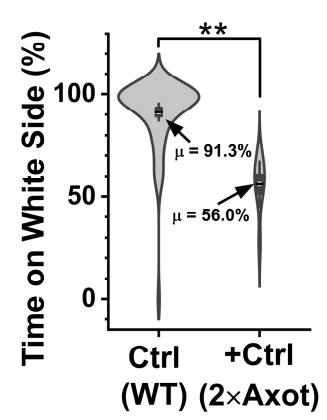


Figure S2. Validation of the behavioral assay. Double axotomy of the optic nerves significantly impacted the background color preference of the tadpoles. Key: **p* < 0.05 (Mann-Whitney test).

experiments, (**Fig. S2**), the mean time tadpoles spent over the preferred white background was ~56% in the positive control group vs. ~91% in the Ctrl. group with this difference amounting to statistical significance in our measurements (Mann-Whitney test, $p = 1.64 \times 10^{-5}$). Representative videos are provided for a Ctrl. (**Video S1**) and a +Ctrl. tadpole (**Video S2**). These results validated the sensitivity and robustness of the behavioral assay to support our studies on tadpole behavior.

The behaviors of experimental and control tadpoles were compared. The biological replicate size for the behavioral assay was N = 16 in the Ctr. group (tadpoles raised from nonmicrosampled embryos) and N = 15 in the experimental group (Exp., tadpoles raised from microsampled embryos). **Figure S3** presents representative images of the tadpoles. Power analysis was performed to compute the power to distinguish the wildtype group from the experimental group. Using two sample t-test ($\alpha = 0.05$, sample size = 60),

the power was 0.08, which was below the acceptable power required to distinguish the two groups (> 0.8). Together with the Mann-Whitney test, these results indicated that microsampling imposed no detectable impact of statistical significance on the background preference of the tadpoles within the tested sensitivity of the behavioral assay.

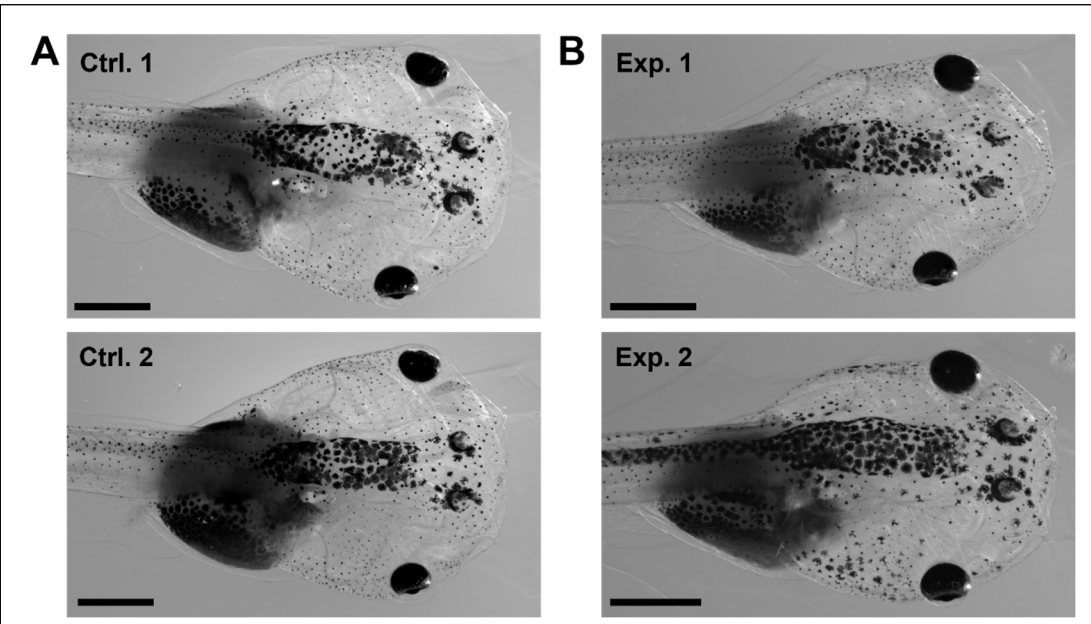


Figure S3. Representative high-resolution images of live tadpoles. Close-ups of tadpoles from **(A)** the control (Ctrl.) and **(B)** the experimental (Exp.) group. Scale bars = 1 mm.

Metabolomic Measurements. Each subcellular metabolite extract was defrosted, and a 10 nL portion was analyzed on a custom-built CE-μESI platform with a high-resolution time-of-flight tandem mass spectrometer. This platform was built and operated according to our established protocols. [4c, 7] The instrument was daily validated for the following analytical figures of merit before analyzing the cell extracts: lower limit of detection, 60 amol (acetylcholine); linear dynamic range of quantification, 4-5 log order (acetylcholine, methionine, and threonine); reproducibility, <1% relative standard deviation (RSD) with nonlinear time alignment^[8] in separation time and <25% RSD in under-the-curve peak area. The experimental settings specific to this study were: CE, 100 cm capillary length and +22.5 kV potential (applied to the capillary inlet); ESI, coaxial sheath-flow CE-ESI interface (blunt-tip metal emitter, 1 µL/min sheath liquid, electrospray at -1,700 V, cone-jet spraying regime); MS, quadrupole orthogonal acceleration time-of-flight mass spectrometer with a collision induced dissociation cell (Impact HD, Bruker Daltonics, Billerica, MS) delivering 40,000 full width at half maximum (FWHM) resolution and <5 mDa m/z accuracy (both single- and tandem stage) using nitrogen gas at 12–18 eV collision energy. Each sample was analyzed in technical duplicate-triplicate.

Proteomic Measurements. Each subcellular protein digest was defrosted and individually reconstituted in 2 μL of aqueous 60% acetonitrile containing 0.05% acetic acid. A 10 nL portion of each protein digest was analyzed on a custom-built CE-nanoESI platform equipped with a quadrupole orbitrap high-resolution mass spectrometer. The instrument was built and operated following our established protocols. ^[9] The platform was daily validated to deliver the following analytical figures of merit before measuring the cell extracts: lower limit of detection, 700 zmol (angiotensin II); linear dynamic range of quantification, 4–5 log-order; reproducibility, <10% RSD in migration time and <25% RSD in signal intensity. The experimental settings specific to this study were: CE, 90 cm capillary length and +18 kV potential for 15 min and +15 kV thereafter (applied to the capillary inlet); CE-nanoESI^[10], electrokinetic pump supplying 10% MeOH (0.05% AcOH) at +800–1,000 V (applied to the sheath reservoir), cone-jet spraying regime confirmed by a long working distance camera (EO-2018C with Mitutoyo Plan Apo objective, Edmund Optics, Barrington, NJ); and MS, quadrupole orbitrap mass spectrometer (Q-Exactive Plus, Thermo Scientific, Milford, MA).

Experimental conditions of data-dependent acquisition were tailored to fast and efficient separation by CE. Survey spectra were recorded at 35,000 FWHM (m/z 200) between m/z 350–1,600 (C-trap maximum injection time, 50 ms; AGC target, 1×10^6 ions). MS² scans were triggered for ion signal intensity exceeding 1.5×10^3 counts when the charge state was between +2-+7 and exhibited peptide-like isotopic distribution. An exclusion list of ~250 vitellogenin (Vtg) peptides was created based on identifications from a whole embryo "pre-run" to help minimize/avoid the sequencing of abundant yolk-related peptide signals. The MS¹ exclusion mass tolerance was 3 ppm. The MS² scans parameters were as follows: mass resolution, 17,500 FHWM (m/z 200); C-trap maximum injection time, 60 ms with AGC target, 5×10^4 counts; dynamic exclusion time and mass tolerance, 9 s and 5 ppm; peptide isolation window, 1 Da; collision parameters, HCD in nitrogen at 28% normalized collision energy (NCE). Each protein digest was measured in technical duplicate-triplicate.

To increase identification numbers using the match between run feature, we also measured cell samples using our CE-nanoESI coupled to a Fusion Lumos quadrupole-linear ion trap-orbitrap tribrid mass spectrometer (Thermo Scientific). MS^1 parameters were as follows: mass analyzer, orbitrap; mass range, m/z 350–1,600; mass resolution; 50,000 FWHM (m/z 200); C-trap maximum injection time, 86 ms; automatic gain control (AGC) target, 1×10^6 ions. MS^2 scans were triggered for ion signal intensity exceeding 1.5×10^3 counts, with charge state between 2–7, and exhibited peptide-like isotopic distribution. The MS^2 scans parameters were as follows: mass analyzer, ion trap; AGC target, 5×10^4 counts; dynamic exclusion time and mass tolerance, 9 s and 5 ppm; peptide isolation window, 1 Da; collision parameters, HCD in nitrogen at 32% normalized collision energy.

Identification and Quantification of Metabolites and Proteins. *Metabolites* were identified and relatively quantified following our established protocols. [4a, 4c, 7] Molecular features (signals with unique m/z vs. migration time values) with $S/N \ge 3$ were surveyed between m/z 50–500 using a semi-automated approach. For each molecular feature, the under-the-curve peak area was integrated, providing a proxy for concentration. These quantitative metadata were imported to MetaboAnalyst version $5.0^{[11]}$ for mean-normalization and log-transformation, then exported for integration with the proteomics metadata, before importing of the unified metabolomic-proteomic metadata for statistical data analysis. Selected molecular features were identified by matching the accurate mass, isotope distribution, CID fingerprint, and migration time of the unknown signal to data available in metabolomics MS-MS/MS databases (Metlin^[12]) or experimentally determined by us in this study or previously^[1,4a].

Proteins were identified and quantified following established protocols. The MS-MS/MS data were matched against the X. laevis proteome using MaxQuant^[13] version 1.6 running the Andromeda search engine. [14] The X. laevis proteome database was custom built by concatenating the mRNA-derived PHROG1r0 database (downloaded from reference^[15]) and the X. laevis SwissProt proteome database (downloaded from UniProt on Oct. 2019). The following search parameters were used: no fixed modification; variable modifications, methionine oxidation, and asparagine and glutamine deamidation; minimum peptide length, 5 amino acids; MS¹ mass deviation, 5 ppm; MS² mass tolerance, 20 ppm for first search and 10 ppm for de novo tolerance; search for common contaminants enabled; match between run enabled with 5 min time shift tolerance. A minimum of one unique peptide was required for successful protein identification. Identified common contaminants were manually excluded from proteins identified or quantified in this study. Peptide and protein identifications were filtered to <1% false discovery rate (FDR) calculated against a reversed-sequence decoy database. Proteins were quantified using the label-free quantification (LFQ) approach in MaxQuant using unique and razor peptides.^[16] Only proteins with less than 50% missing LFQ values across all the samples were considered as successfully quantified and used for statistical and pathway analysis. Protein LFQ values were mean-normalized and log-transformed in MetaboAnalyst version 5.0^[11], then exported for integration with the metabolomics data, before importing of the unified metadata for statistical analysis.

Experimental Design and Statistics. For each portion of this study, the number of necessary technical and biological replicates for statistical significance were determined based on a pilot study and the analytical performance metrics of the custom-built CE-ESI-MS platform. Statistical, multivariate, and joint pathway analyses were performed in MetaboAnalyst 5.0. Statistical significance was marked at $p \le 0.05$ (paired student t-test for normally distributed data). Power analysis (two-sample t-test, alpha value 0.05, hypothetical sample size N = 60), Student's t-test (parametric, normally distributed data), Mann-Whiney test (nonparametric, non-paired data), and Wilcoxon signed rank test (nonparametric, paired data) were performed in OriginPro 2020b (OriginLab Corp., Northampton, MA). For pathway enrichment analysis, gene and metabolite centered pathway was chosen. Enrichment was measured using hypergeometric test, topology was calculated by degree of centrality, and the integration method used was combined p-value (overall).

REFERENCES

- [1] E. P. Portero, P. Nemes, *Analyst* **2019**, *144*, 892-900.
- [2] H. L. Sive, R. M. Grainger, R. M. Harland, *Early development of Xenopus laevis:* a laboratory manual, Cold Spring Harbor Laboratory Press, **2000**.
- [3] S. A. Moody, M. J. Kline, *Anat. Embryol.* **1990**, *182*, 347-362.
- [4] (a) R. M. Onjiko, E. P. Portero, S. A. Moody, P. Nemes, *Anal. Chem.* 2017, 89, 7069-7076; (b) R. M. Onjiko, D. O. Plotnick, S. A. Moody, P. Nemes, *Anal. Methods* 2017, 9, 4964-4970; (c) R. M. Onjiko, E. P. Portero, S. A. Moody, P. Nemes, *J Vis Exp* 2017, e56956; (d) C. Lombard-Banek, S. A. Moody, M. C. Manzin, P. Nemes, *Anal. Chem.* 2019, 91, 4797-4805.
- [5] R. M. Onjiko, S. E. Morris, S. A. Moody, P. Nemes, *Analyst* 2016, 141, 3648-3656.
- [6] A. S. Viczian, M. E. Zuber, *J Vis Exp* **2014**, e51726.
- [7] R. M. Onjiko, S. A. Moody, P. Nemes, *Proc. Natl. Acad. Sci. U. S. A.* **2015**, *112*, 6545-6550.
- [8] P. Nemes, S. S. Rubakhin, J. T. Aerts, J. V. Sweedler, *Nat. Protoc.* 2013, 8, 783-799.
- [9] (a) C. Lombard-Banek, S. A. Moody, P. Nemes, *Angew. Chem. Int. Edit.* 2016, 128, 2500-2504; (b) C. Lombard-Banek, S. Reddy, S. A. Moody, P. Nemes, *Mol. Cell. Proteomics* 2016, 15, 2756-2768; (c) C. Lombard-Banek, S. A. Moody, P. Nemes, *Front. Cell Dev. Biol.* 2016, 4, 100.
- [10] L. Sun, G. Zhu, Y. Zhao, X. Yan, S. Mou, N. J. Dovichi, *Angew. Chem. Int. Edit.* **2013**, *52*, 13661-13664.
- [11] J. G. Xia, D. S. Wishart, *Nat. Protoc.* **2011**, *6*, 743-760.
- [12] J. Xue, C. Guijas, H. P. Benton, B. Warth, G. Siuzdak, *Nat. Methods* **2020**, *17*, 953–954.
- [13] J. Cox, M. Mann, *Nat. Biotechnol.* **2008**, *26*, 1367-1372.
- [14] J. Cox, N. Neuhauser, A. Michalski, R. A. Scheltema, J. V. Olsen, M. Mann, *J. Proteome Res.* **2011**, *10*, 1794-1805.
- [15] M. Wuhr, R. M. Freeman, Jr., M. Presler, M. E. Horb, L. Peshkin, S. P. Gygi, M. W. Kirschner, *Curr. Biol.* 2014, 24, 1467-1475.

[16] J. Cox, M. Y. Hein, C. A. Luber, I. Paron, N. Nagaraj, M. Mann, *Mol. Cell. Proteomics* **2014**, *13*, 2513-2526.